Electronic Supplementary Information

Decrypting the hydrogen evolution in alkaline water with newfangled magnetoactive cobalt(II) complexes-driven cobalt oxide electrocatalysts

Subhajit Saha,[a]Nilankar Diyali,[a]Sangharaj Diyali,[a]Subhra Jyoti Panda,[b]Mainak Das,[c]Sobhna Acharya,[d] Prafullya Kumar Mudi,[a]Monika Singh,[d] Partha Pratim Roy,[c] Chandra Shekhar Purohit,[b] and Bhaskar Biswas[a]*

---

[a]*Department of Chemistry, University of North Bengal, Darjeeling-734013, India.*

[b] *Department of Chemical Sciences, National Institute of Science Education and Research, Bhubaneswar 752050, India.*

[c]*Department of Physics, Jadavpur University, Kolkata-700032, India.*

[d]*Energy and Environment Unit, Institute of Nano Science and Technology, Mohali 140306, India*

Table of Content		
		Page No.
A.	**Experimental**	**S1-S8**
	1. Synthetic Procedure	**S1-S2**
	1.1. Chemicals	**S1**
	1.2. Synthesis of **Co^{mono}**	**S1**
	1.3. Synthesis of **Co^{di}**	**S2**
	2. FT-IR analysis	**S2**
	3. Physical measurements	**S2-S3**
	4. X-ray structural studies and refinement	**S3-S4**
	5. Electrical measurement	**S4-S6**
	5.1. Fabrication of Schottky Device	**S4**
	5.2. Electrical Characterization	**S4-S6**
	6. Electrochemistry	**S6-S8**
	6.1. Electrochemical measurement	**S6-S7**
	6.2. Electrode preparation	**S7**
	6.3. Determined the Electrochemical Active Surface Area	**S7**
	6.4. Roughness Factor	**S7**
	6.5. Calculation of active sites and turnover frequency	**S8**
B.	**Figures**	**S9-S22**
	S1: FT-IR spectra of the **Co^{mono}** and **Co^{di}** .	**S9**
	S2: UV spectra of H**L**, **Co^{mono}** , and **Co^{di}** .	**S9**
	S3: EDX spectrum of **Co^{mono}** .	**S10**
	S4: EDX spectrum of **Co^{di}**.	**S10**

	S5: **(a)** Wide scan XPS (X-ray Photoelectron Spectrometry) spectra of **Co^{mono}**; High-resolution XPS spectrum of **(b)** S 2p, **(c)** O 1s **(d)** N 1s, **(e)** Co 2p and **(f)** C 1s.	**S11**
	S6: (a) Wide scan XPS (X-ray Photoelectron Spectrometry) spectra of **Co^{di}**; High-resolution XPS spectrum of **(b)** O 1s, **(c)** N 1s, **(d)** Co 2p and **(e)** C 1s.	**S11**
	S7: I-V characteristics plot for **Co^{mono}** and **Co^{di}**. Inset: Logarithmic current vs voltage plot.	**S12**
	S8: dV/d(lnI) vs. I and H(I) vs. I curve for **Co ^{mono}**	**S12**
	S9: dV/d(lnI) vs. I and H(I) vs. I curve for **Co ^{di}**	**S13**
	S10: Capacitance versus frequency plot for **Co ^{di}**	**S13**
	S11: Capacitance versus frequency plot for **Co ^{mono}**	**S14**
	S12: Nyquist plot for **Co^{mono}** and **Co^{di}** complexes	**S14**
	S13: CV plot of **Co ^{mono}** (black) and **Co ^{di}** (red) in ACN medium with a scan rate of 100 mV/s between 0 V to -1.2 V (V vs. Ag wire).	**S15**
	S14: CV plot of H**L** in ACN medium with a scan rate of 100 mV/s between 0 V to -1.2 V (V vs. Ag wire).	**S15**
	S15: Comparison of PXRD patterns of simulated **Co ^{mono}** (black), **Co ^{mono}** after sonication in the presence of Nafion and ethanol (purple), **Co ^{mono}** after soaking in 0.1 M KOH for 24h (dark cyan).	**S16**
	S16: Comparison of PXRD patterns of simulated **Co ^{di}** (black), **Co ^{di}** after sonication in the presence of Nafion and ethanol (purple), **Co ^{di}** after soaking in 0.1 M KOH for 24h (dark cyan).	**S16**
	S17: Plot of current vs potential at different scan rates for the determination of double layer capacitance at the non-Faradic region for **Co ^{mono}.**	**S17**
	S18: Current vs.scan rate plot for **Co^{mono}**	**S17**
	S19: Controlled potential electrolysis of **Co^{mono}** (black), **Co^{di}** (red) and bare glassy electrode (GCE, blue) at -0.49V vs. RHE for 6000s.	**S18**
	S20: LSV of **Co^{mono}** before and after CPE in N_2-saturated water using 0.1 M KOH as supporting electrolyte at a scan rate of 5 mV/s.	**S18**

	S21: LSV of **Co^{di}** before and after CPE in N_2-saturated water using 0.1 M KOH as supporting electrolyte at a scan rate of 5 mV/s.	**S19**
	S22: Controlled potential electrolysis (CPE) of **Co^{mono}** performed at –0.37 V (V vs. RHE) in N_2-saturated water using 0.1 M KOH as supporting electrolyte to determine the corresponding faradic efficiency for hydrogen production.	**S19**
	S23: Multicycle CVs of **Co ^{mono}** at 1000mV/s scan rate, between 0.96 to -0.84(V vs RHE).	**S20**
	S24: Multicycle CVs of **Co ^{di}** at 1000mV/s scan rate, between 0.96 to -0.84(V vs RHE).	**S20**
	S25: High-resolution XPS spectrum of Co 2p; **a)** post-electrocatalyst of **Co^{mono}**, and **b)** post-electrocatalyst of **Co^{di}**.	**S21**
	S26: A comparison of the PXRD pattern of post-CPE electrocatalysts, **Co^{mono}** and **Co^{di}** with the PXRD pattern of the standard Co_3O_4 (JCPDS: 00-042-1467)	**S21**
	S27: SEM images of post-CPE recovered electrocatalysts	**S22**
	S28: CPE of **Co^{mono}** and wash test of blank working electrode (GC) in 0.1M KOH solution for 6000 sec at -0.49 (V vs RHE).	**S22**
	S29: CPE of **Co ^{di}** (red) and wash test of blank working electrode (GC) (blue) in 0.1M KOH solution for 6000 sec at -0.49 (V vs RHE).	**S23**
C.	**Tables**	**S24-S30**
	S1: Crystallographic parameters of **Co^{mono}** and **Co^{di}**	**S24-S25**
	S2: Bond distances and bond angles of **Co^{mono}**	**S25**
	S3: Bond distances and bond angles of **Co^{di}**	**S26**
	S4: Hydrogen bond lengths (Å) and angles (°) for **Co^{mono}**	**S27**
	S5: Hydrogen bond lengths (Å) and angles (°) for **Co^{di}**	**S27**
	S6: Comparison of magnetic properties of reported dinuclear Co (II) Complexes	**S28**
	S7: Temperature-dependent conductivity of **Co^{mono}** and **Co^{di}**	**S28**
	S8: Schottky Diode Parameters	**S29**
	S9: SCLC/Charge Transport Parameters	**S29**
	S10: Electrochemical parameter	**S30**
	S11: Electrochemical parameters before and after CPE	**S30**
E.	**References**	**S31-S33**

A. Experimental

1. Synthetic procedure

1.1. Chemicals

All chemicals and solvents used in the synthesis were the analytical reagent grade (AR), and of the highest purity available. >98.0% pure 2-methoxyaniline (TCI, Japan), >97.0% Ortho-Vanillin (TCI, Japan), Cobalt (II) perchlorate hexahydrate (Sigma-Aldrich, USA), NH_4SCN (SRL, India), Nafion® 117 solution (Sigma-Aldrich, USA) and Potassium hydroxide pellets (SRL, India) were purchased from monetary outlets. All the solvents were used as received without further purification.

1.2. Synthesis of Co^{mono}

The ligand (**HL**) was synthesized following the method our group had previously reported.[1] The $\mathbf{Co^{mono}}$ complex was synthesized by stirring **HL** with $Co(ClO_4)_2,6H_2O$ followed by adding NH_4NCS in 2:1:2 in methanol medium. The **HL** (0.2mmol) was dissolved in 10 ml of methanol, and after a few minutes of stirring, a methanolic solution of Co $(ClO_4)_2,6H_2O$ (0.1mmol) was added to the mixture. Then, after the solution of NH_4NCS was added dropwise, the resultant solution was stirred for 30min. After that, the final reaction mixture was filtered off and kept for slow evaporation under ambient conditions. After a few days, the reddish-brown single crystal was obtained. The molecular formula $\mathbf{C_{32}H_{30}N_4O_6S_2Co}$. Yield ~ 64% (with respect to metal salt). Elemental analysis: Anal. Calc C:55.73, H 4.38, N 8.12 %. Found 55.69, H 4.41, 8.09 %. IR (KBr, cm^{-1}): 3435(O^-…NH^+) ,2072 (SCN),1636(C=N). UV-Vis (λ, nm, ACN):270(ε =15679.31),333(ε =18965.52),434(ε =3171.03),636(ε =448.62).

1.3. Synthesis of Co^{di}

Ligand HL (0.2mmol) was dissolved in 10 ml of methanol and stirred for a few minutes in slightly warm (40°C) conditions. Then, a methanolic solution of Co $(ClO_4)_2$,$6H_2O$ (0.1mmol) was dissolved in the reaction solution and kept for 30 min in stirring conditions. After that, the resulting solution was kept for slow evaporation under ambient conditions. After 7 days, red colour single crystal was obtained. Molecular formula [$\mathbf{C_{46}H_{46}N_3O_{10}Co_2}$] $\mathbf{ClO_4}$. Yield ~ 55% (with respect to metal salt). Elemental Calc C: 54.26, H 4.55, N4.13 %. Found, C 54.30, H 4.52, N 4.15 %. IR (KBr, cm^{-1}): 1613(C=N), 1085(ClO_4). UV-Vis (λ, nm, ACN): 292(ε =26078.63), 331(ε =32493.57),409(ε =18358.37).

Caution! *Perchlorate salts of metal ions are potentially explosive. Only a small amount of material should be prepared, and it should be handled with care.*

2. FT-IR spectral analysis

For $\mathbf{Co^{mono}}$, the stretching frequency at 2072 cm^{-1} is assignable to the coordinated SCN^- while the −C=N− stretching vibration is evident at 1636 cm^{-1}. Another broad peak at ~3435 cm^{-1} is assignable to the presence of intramolecular hydrogen bonding of the Zewitter ion ligand (O^- …NH^+) in $\mathbf{Co^{mono}}$.[2] On the contrary, the IR spectrum of $\mathbf{Co^{di}}$ shows a characteristic stretching vibration at 1613 cm^{-1} denoting the coordination from the azomethine-N of the ligand.[3] The presence of perchlorate ion is also evident by the peak at 1085 cm^{-1} in the complex, $\mathbf{Co^{di}}$. Noteworthy, the characteristic peaks at ~2925 cm^{-1} for both the complexes point out the ligand centric $-CH_2-$ vibration of $-OCH_3$ groups.[4]

3. Physical measurements

FT-IR spectra of both the Co complex ($\mathbf{Co^{mono}}$ and $\mathbf{Co^{di}}$) were recorded by using an FTIR-8400S SHIMADZU spectrometer in the range of 400-4000 cm^{-1}. The elemental analysis of the synthesized compounds was executed with the help of a Perkin Elmer 2400 CHN

microanalyzer. A HITACHI U-2910 spectrophotometer was used to measure steady-state absorption. The morphology and structural characteristics of the synthetic compounds were determined by powder X-ray diffractometer (Rigaku SmartLab) using Cu-K α radiation ranging from 10°-80°. The size and shape of the particles were assessed through scanning electron microscopy (JSM IT500HR, Japan) images. Electron dispersive X-ray (EDX) spectral analysis was also carried out to reveal the % elemental contribution and purity of the materials. A K-Lyte electrochemical workstation consisting of a glassy-carbon working electrode, Pt counter electrode, and Ag/AgCl reference electrode (saturated with KCl) was employed to study the electrochemical analysis of the compounds. Gas chromatography experiments were performed on an HP (Agilent) 5890 series II instrument with an ECD detector. The remainder of the gas in the headspace was analysed with a PGas-22 H_2 gas detector. Temperature-dependent magnetic susceptibility measurement was carried out on a SQUID Magnetometer (Quantum Design's MPMS 3, USA) ranging from 4.8 to 300 K under a 1.0 kOe field. X-ray Photoelectron Spectrometry (XPS) analysis was carried out using ESCALab:220-IXL with Mg Kα non-monochromatic X-ray beam. The valence states of the elements were determined by the NEXSA X-Ray Photoelectron Spectrometer (XPS) system of Thermo Scientific.

4. X-ray structural studies and refinement

Suitable single crystals of **Co^{mono}** and **Co^{di}** were selected for single-crystal X-ray diffraction studies. The structural diffraction data were collected on a Bruker-Kappa APEX II CCD diffractometer equipped with a 1 K charge-coupled device (CCD) area detector employing a graphite monochromated Mo-Ka radiation (k¼ 0.71073 A) ˚ at 100.0(2) K. The cell parameters and the reduction and correction of the collected data were determined by SMART SAINTPLus software, respectively,[5] followed by SADABS absorption corrections.[6] Finally, the structure was solved by direct method with the SHELXL-97 program package. The refinement by full-matrix least-squares method was executed on all F2 data with SHELXL-97.[7] For all non-

hydrogen atoms, anisotropic refinement was performed. Subsequently, the additional hydrogen atoms were positioned by the riding model.

5. Electrical measurement

5.1. Fabrication of Schottky Device

To fabricate the Schottky device, at first, Indium Tin Oxide (ITO) coated glass substrate was cleaned by acetone, distilled water, and isopropanol repeatedly and sequentially in an ultrasonication bath for 30 min. At the same time, a well-dispersed solution of the **Co^{di}** and **Co^{mono}** in N N-dimethyl formamide (DMF) medium was prepared and spin-coated onto the pre-cleaned ITO-coated glass at 800 rpm for 1 min with the help of SCU 2700 spin coating unit. This spin-coating step was repeated 5 times. After drying in a vacuum, the film thickness was measured as 1 μm by a surface profiler. Aluminium (Al) electrodes were deposited onto the film by a Vacuum Coating Unit 12A4D of HINDHIVAC under a pressure of 10^{-6} mbar. The area of the Al electrodes was maintained as 7.065×10^{-6} m^2 by the shadow mask. The current-voltage measurements of the fabricated device with **Co^{di}** and **Co^{mono}** were carried out by a Keithley 2635B source meter interfaced with PC by a two-probe technique between the voltage range -5V to +5V at room temperature.

5.2. Electrical Characterization

The Thermionic Emission (TE) theory is adopted to get more insights of the charge transport mechanism in the devices.[8] According to TE theory, the current of a diode can be expressed as the following equations.[9]

$$I = I_0 \exp\left(\frac{qV}{\eta kT}\right)\left[1 - \exp\left(-\frac{qV}{\eta kT}\right)\right] \quad \text{..... (S1)}$$

Where,

$$I_0 = AA^*T^2 exp\left(-\frac{q\phi_B}{kT}\right) \quad \text{..... (S2)}$$

$$\phi_B = \frac{kT}{q} ln\left(\frac{AA^*T^2}{I_0}\right) \text{.....(S3)}$$

Where, I_0 indicates the saturation current, q represents the electronic charge, k is the Boltzmann constant, T is the temperature in Kelvin, V is the forward bias voltage, η is the ideality factor, ϕ_B is the effective barrier height at zero bias, A is the diode area (7.065×10^{-6} m^2), A^* is the effective Richardson constant (1.20×10^6 $Am^{-2}K^{-2}$). From Cheung, the forward bias I-V characteristics in term of series resistance can be expressed as. [10]

$$I = I_0 exp\left[\frac{q\left(V - IR_S\right)}{\eta kT}\right] \text{.....(S4)}$$

Where, the IR_S term represents the voltage drop across series resistance of device. In this circumstance, the values of the series resistance can be determined from following functions using equation (S5 & S6).[11]

According to Cheung's model:

$$\frac{dV}{dln(I)} = \left(\frac{\eta kT}{q}\right) + R_S I \text{ ..... (S5)}$$

$$H(I) = R_S I + \eta\phi_B \text{.....(S6)}$$

and H(J) can be expressed as:

$$H(I) = V - \left(\frac{\eta kT}{q}\right) ln\left(\frac{I}{AA^*T^2}\right) \text{ ..... (S7)}$$

The Mott-Gurney(SCLC) equation[12]

$$\mathbf{I = \frac{9\mu_{eff}\varepsilon_0\varepsilon_r A}{8}\left(\frac{V^2}{d^3}\right)} \quad \text{..... (S8)}$$

Where, the symbols take their own representation. The dielectric constant of two materials are measured from capacitance vs. frequency plot (C-f) by the equation.[13]

$$\mathbf{\varepsilon_r = \frac{Cd}{\varepsilon_0 A}} \quad \text{..... (S9)}$$

Transit time (τ) is the time at which time a carrier travels from anode to cathode. It is the sum of the average time spent by an electron as a free carrier plus the total time spent in the tarp. The transit time (τ) is expressed by the following equation.[14]

$$\mathbf{\tau = \frac{9\varepsilon_0\varepsilon_r A}{8d}\left(\frac{V}{I}\right)} \quad \text{..... (S10)}$$

The longer transit time indicates a higher trapping probability.[15]

6. Electrochemistry

6.1. Electrochemical Measurements

The electrochemical studies were performed by using K-Lyte electrochemical workstation. In the three electrodes system, a glassy carbon electrode (GCE, 3 mm diameter) was used as a working electrode, platinum wire as a counter electrode, and Ag/AgCl as a reference electrode (saturated with KCl). The GCE was polished first. The disk surface was made wet with distilled water, followed by making a slurry of alumina powder of size 0.05 microns using distilled water on the pad (polishing kit), then polishing the electrode and interspersed by washings with distilled H_2O. All the electrochemical glassware was immersed in concentrated H_2SO_4 to

remove the impurities. Finally, they were washed with water, followed by overnight oven drying. All the electrochemical measurements were performed at room temperature.

The potential region was swept from 0.0V to -1.8V (vs. Ag/AgCl) at the scan rate of 5 mVs^{-1}. All the potentials in this study were given with respect to a reversible hydrogen electrode (RHE) by using the Nernst equation $E(RHE) = E^0(Ag/AgCl) + E(Ag/AgCl) + 0.059*pH$. All the data were corrected for *iR* loss.

6.2. Electrode preparation

3 mg of pure catalyst were taken into a 2mL vial and 20 μl Nafion (5 wt.%, Sigma Aldrich), 1980µl EtOH (ethanol) were added to the 2ml vial. Then, the solution was left for 20 min sonication to form homogenous ink (low-power sonicator,40 Hz). Then 10 μl ink was drop cast into the GCE and dried at room temperature for 1 day. The mass loading was deceived as 0.212 mg cm^{-2}.

6.3. Determined the Electrochemical Active Surface Area (ECSA)

The value of ECSA can be calculated with the help of electrochemical double-layer capacitance (C_{dl}) by the following equation

$$ECSA = C_{dl}/C_s \quad \text{(S11)}$$

Where C_s represent specific conductance.

6.4. Roughness Factor (RF)

The roughness factor for the catalyst is calculated by the following equation:

$$RF = \frac{ECSA}{Electrode\ geometrial\ area} \quad \text{(S12)}$$

There is no unit of roughness factor.

6.5. Calculation of active sites and turnover frequency (TOF)

The active sites and turnover frequency (TOF) were calculated for **Co ^{mono}** and **Co^{di}** following the equations. Considering the one-electron reduction process from the CV, the absolute components of voltammetric charges (cathodic and anodic) were examined by analysing the area of the curve of complex **Co ^{mono}** and **Co$^{di.}$** Further, the active sites **(n)** of the heterogenous catalyst were calculated in mol^{-1}.

$$\boldsymbol{Charge\ (Q) = \frac{Area\ of\ the\ curve}{2\times Scan\ rate}} \quad \text{……(S13)}$$

$$\mathbf{n = \frac{Q}{2\times F}} \quad \text{…… (S14)}$$

The turnover frequency (in s^{-1}) per-sites were calculated using the equation given below:

$$\boldsymbol{TOF = \frac{I}{F\ n}\frac{1}{2}} \quad \text{…… (S15)}$$

Where ***I*** is current (in A) during the LSV, **F** is Faraday constant (in C mol^{-1}), ***n*** is the number of active sites (in mol) and the factor ½ represents the two-electron process in hydrogen production.

B. Figures

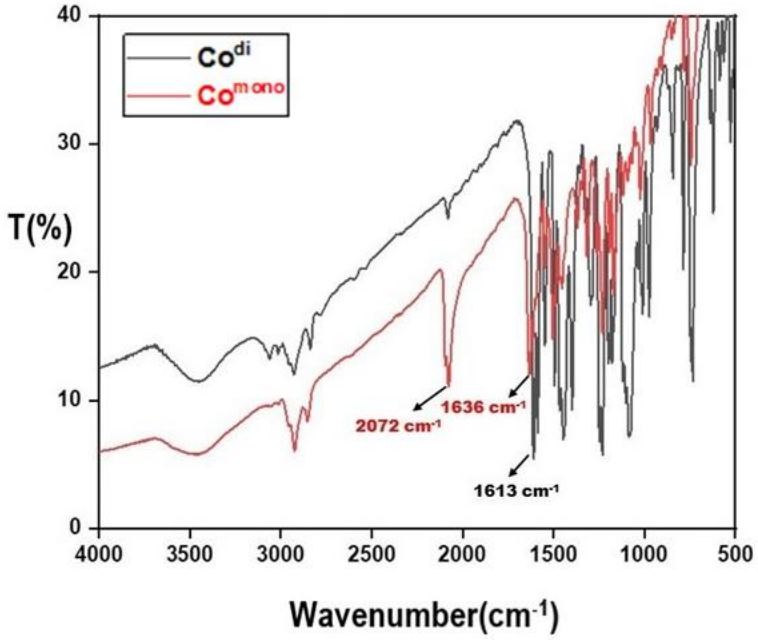

Figure S1: FT-IR spectra of the **Co^{mono}** (red) and **Co^{di}** (black).

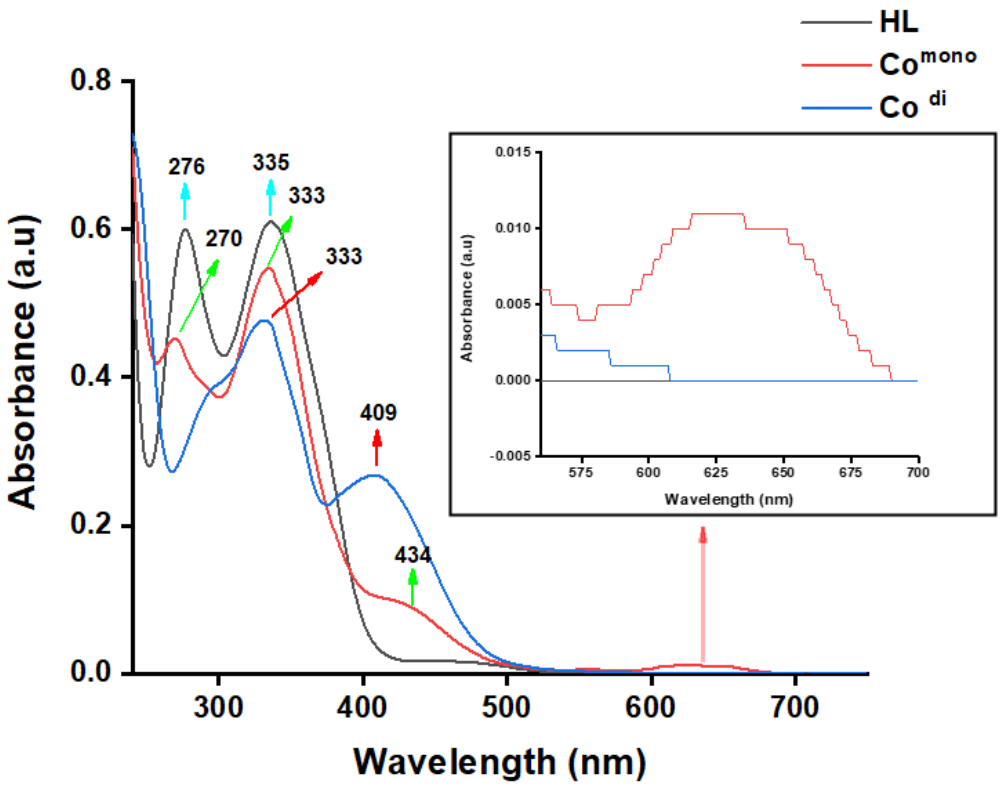

Figure S2: UV spectra of H**L**(black), **Co^{mono}** (red), and **Co^{di}** (blue)**.**

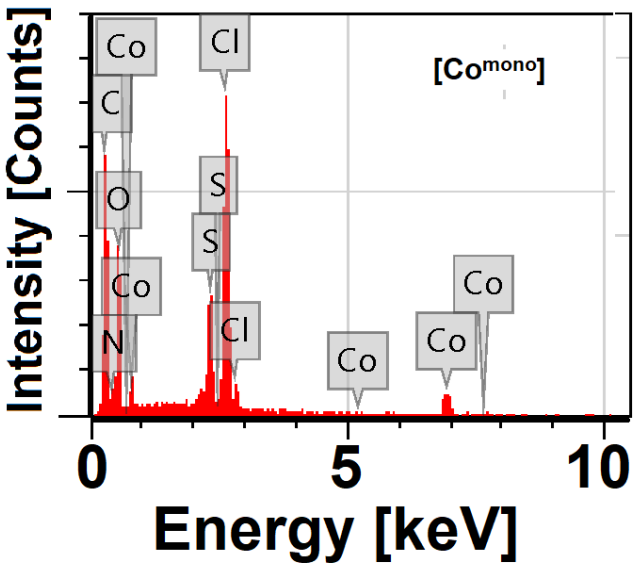

Figure S3: EDX spectrum of **Co^{mono}**.

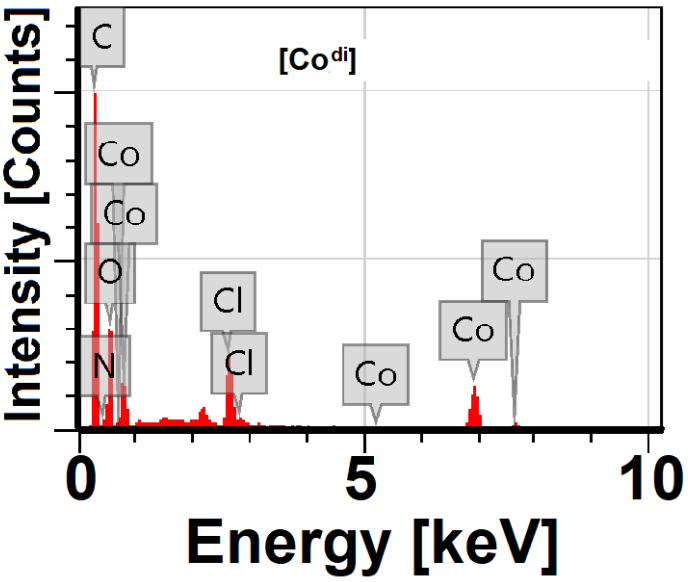

Figure S4: EDX spectrum of **Co^{di}**.

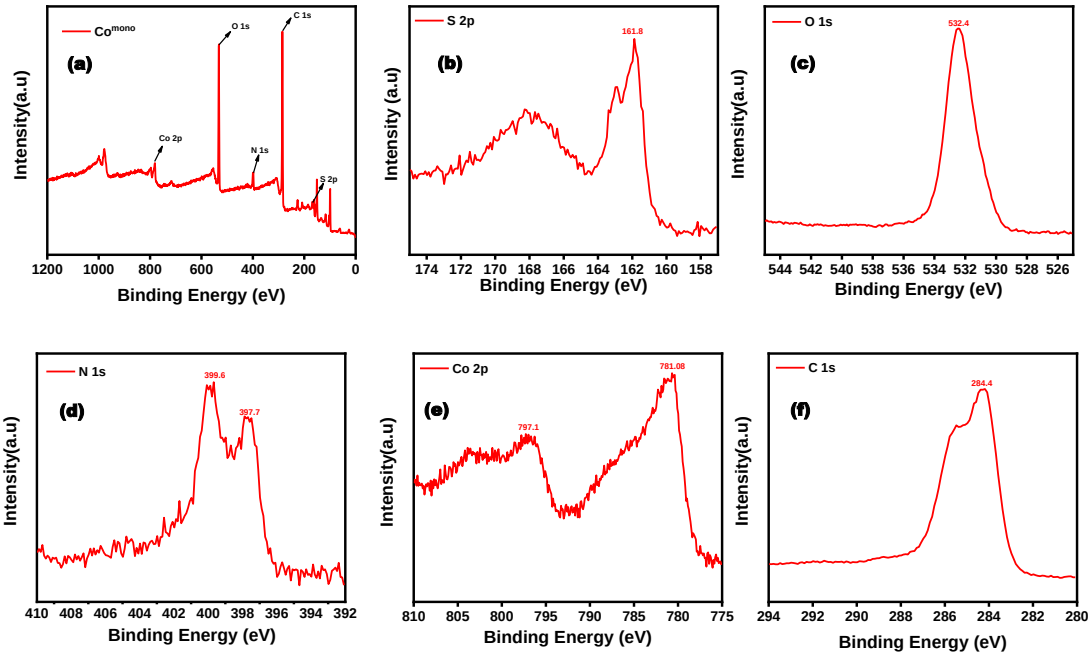

Figure S5: (a) Wide scan XPS (X-ray Photoelectron Spectrometry) spectra of **Co^{mono}**; High-resolution XPS spectrum of **(b)** S 2p,**(c)** O 1s ,**(d)** N 1s, **(e)** Co 2p and **(f)** C 1s.

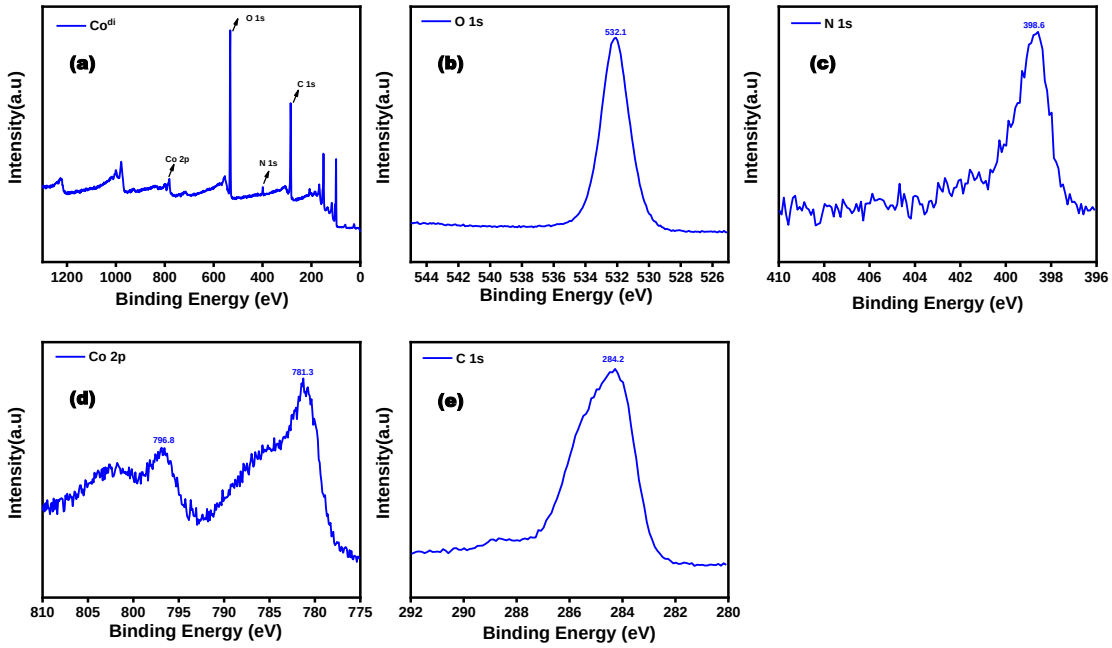

Figure S6: (a) Wide scan XPS (X-ray Photoelectron Spectrometry) spectra of **Co^{di}**; High-resolution XPS spectrum of **(b)** O 1s, **(c)** N 1s, **(d)** Co 2p and **(e)** C 1s.

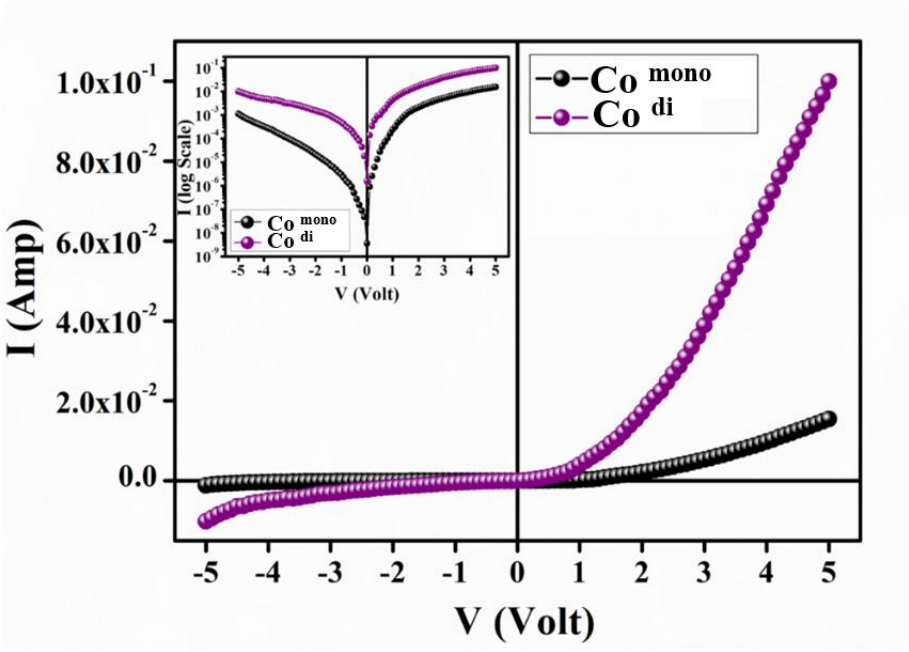

Figure S7: I-V characteristics plot for **Co^{mono}** (black) and **Co^{di} (**violet). Inset: Logarithmic current vs voltage plot.

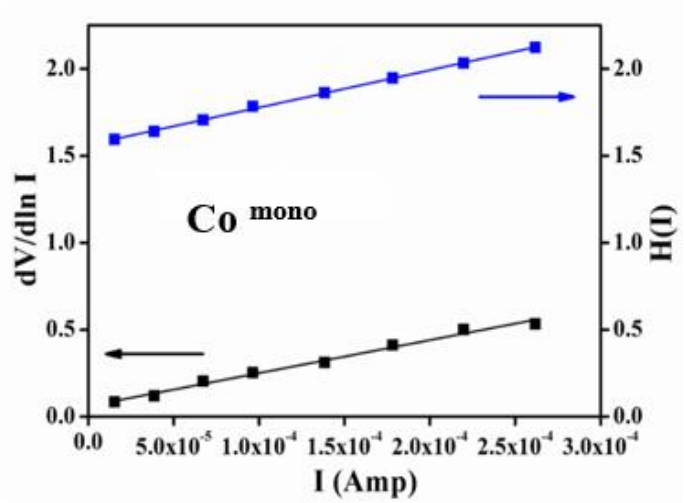

Figure S8: dV/d(lnI) vs. I and H(I) vs. I curve for **Co^{mono}**.

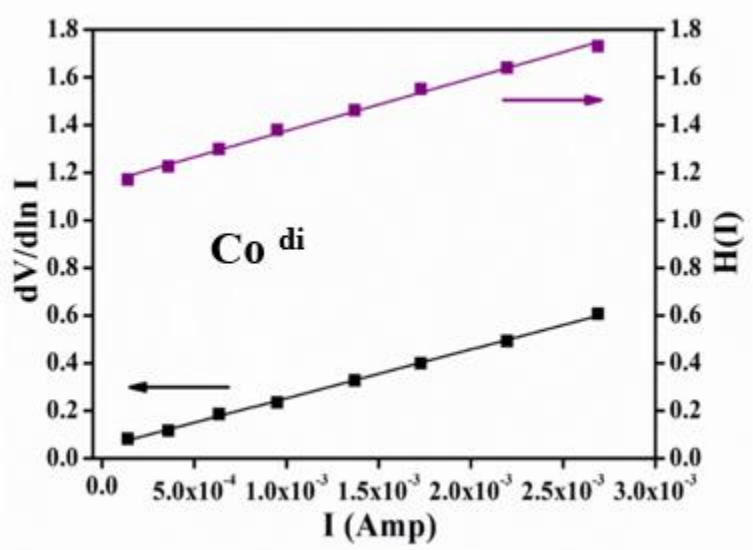

Figure S9: dV/d(lnI) vs. I and H(I) vs. I curve for **Co** [di].

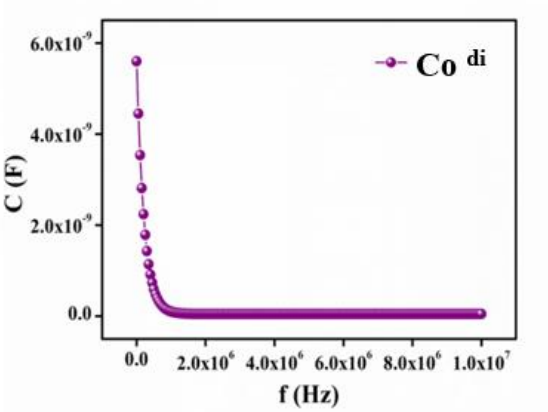

Figure S10: Capacitance versus frequency plot for **Co** [di].

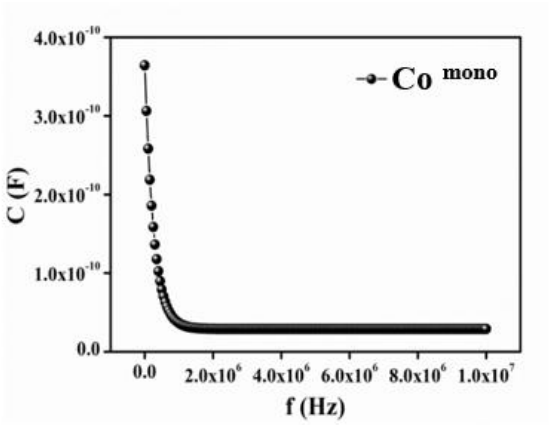

Figure S11: Capacitance versus frequency plot for **Co** **mono**.

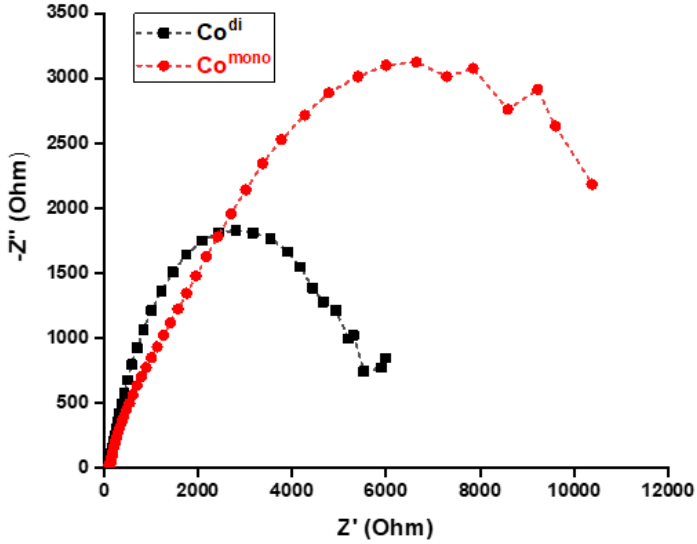

Figure S12: Nyquist plot for **Co**^{mono} (red) and **Co**^{di} **(**black) complexes.

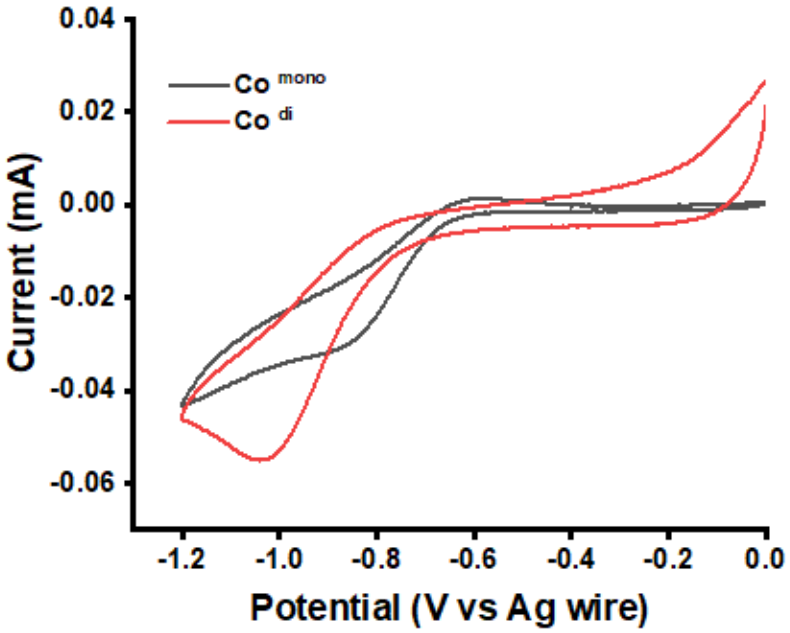

Figure S13:CV plot of **Co** ^{mono} (black) and **Co**^{di} (red) in ACN medium with a scan rate of 100 mV/s between 0 V to -1.2 V (V vs. Ag wire).

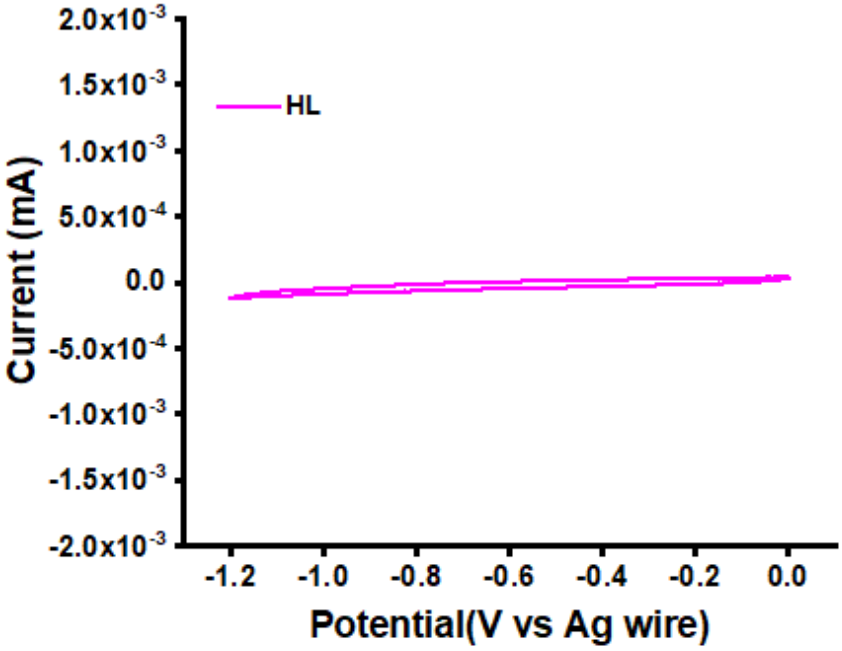

Figure S14: CV plot of H**L** in ACN medium with a scan rate of 100 mV/s between 0 V to -1.2 V (V vs. Ag wire).

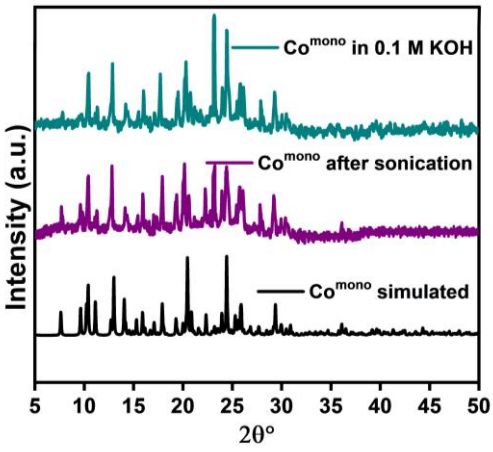

Figure S15: Comparison of PXRD patterns of simulated **Co** ^{mono} (black), **Co** ^{mono} after sonication in the presence of Nafion and ethanol (purple), **Co** ^{mono} after soaking in 0.1 M KOH for 24h (dark cyan).

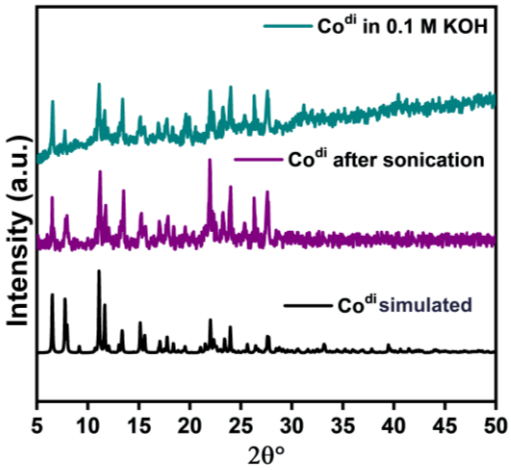

Figure S16: Comparison of PXRD patterns of simulated **Co** ^{di} (black), **Co** ^{di} after sonication in the presence of Nafion and ethanol (purple), **Co** ^{di} after soaking in 0.1 M KOH for 24h (dark cyan).

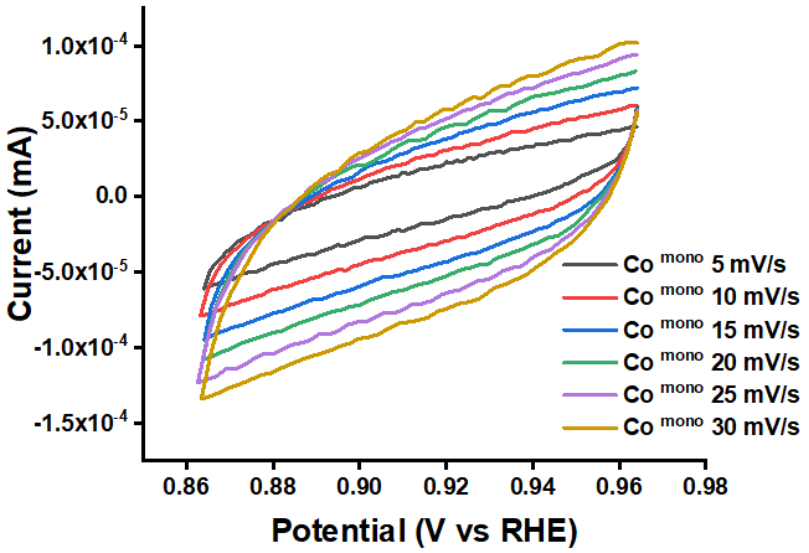

Figure S17: Plot of current vs potential at different scan rates for the determination of double layer capacitance at the non-Faradic region for **Co** $^{\textbf{mono}}$.

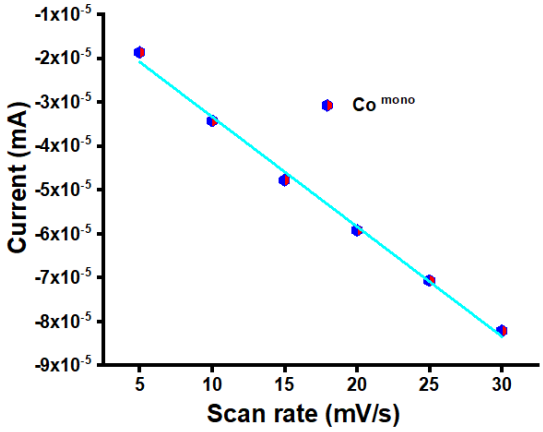

Figure S18: Current vs scan rate plot for **Co** $^{\textbf{mono}}$.

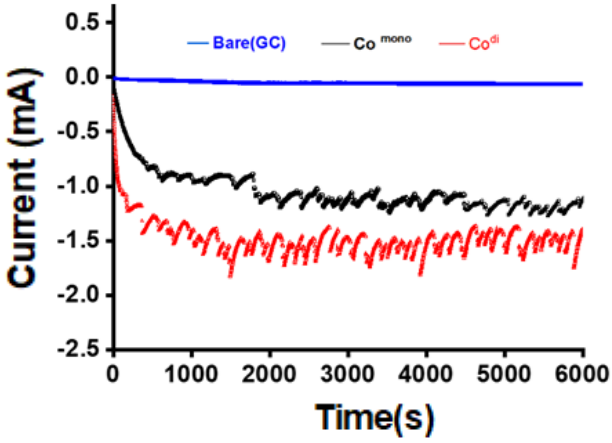

Figure S19: Controlled potential electrolysis of **Co^{mono}** (black), **Co^{di}** (red) and bare glassy electrode (GCE, blue) at -0.49V vs. RHE for 6000s.

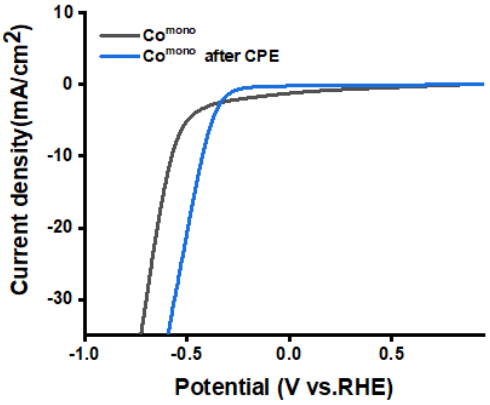

Figure S20: LSV of **Co^{mono}** before (black) and after (blue) CPE in N_2-saturated water using 0.1 M KOH as supporting electrolyte at a scan rate of 5 mV/s.

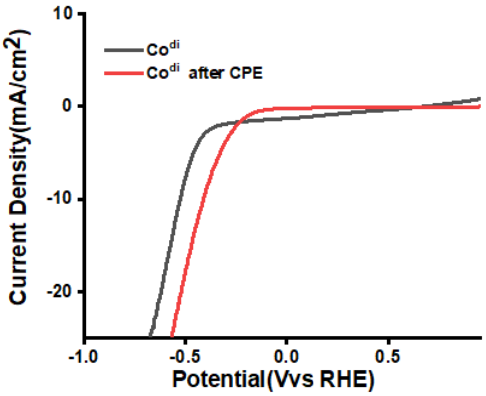

Figure S21: LSV of **Co^{di}** before (black) and after (red) CPE in N_2-saturated water using 0.1 M KOH as supporting electrolyte at a scan rate of 5 mV/s.

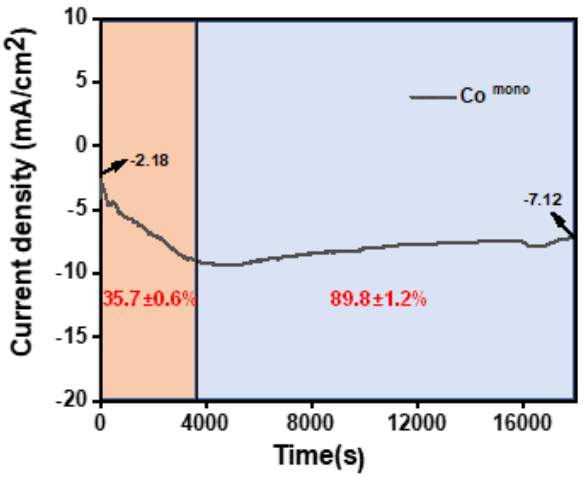

Figure S22: Controlled potential electrolysis (CPE) of **Co^{mono}** performed at -0.37 (V vs. RHE) for 18000 s (5h) in N_2-saturated water using 0.1 M KOH as supporting electrolyte to determine the corresponding Faradic Efficiency for hydrogen production.

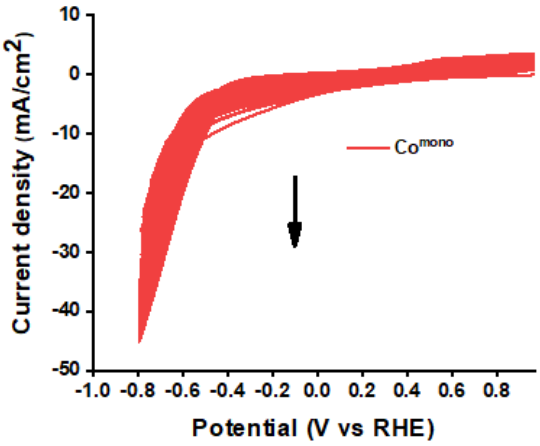

Figures S23: Multicycle CVs (500-cycle) of **Co ^{mono}** at 1000mV/s scan rate, between 0.96 to -0.84(V vs RHE).

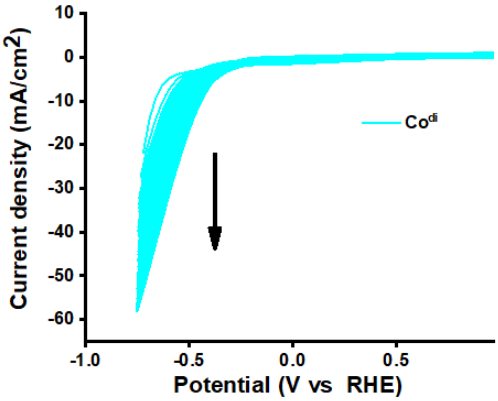

Figures S24: Multicycle CVs (500-cycle) of **Co ^{di}** at 1000mV/s scan rate, between 0.96 to -0.84(V vs RHE).

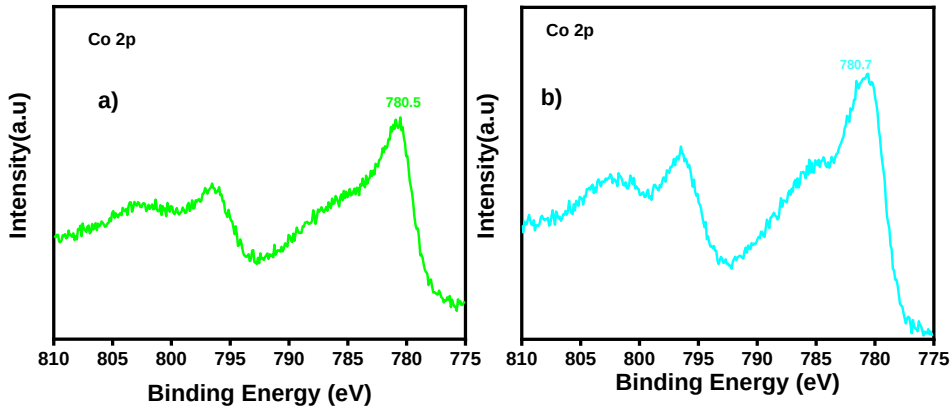

Figure S25: High-resolution XPS spectrum of Co 2p; **a)** post-electrocatalyst of **Co^{mono}**; **b)** post-electrocatalyst of **Co^{di}**.

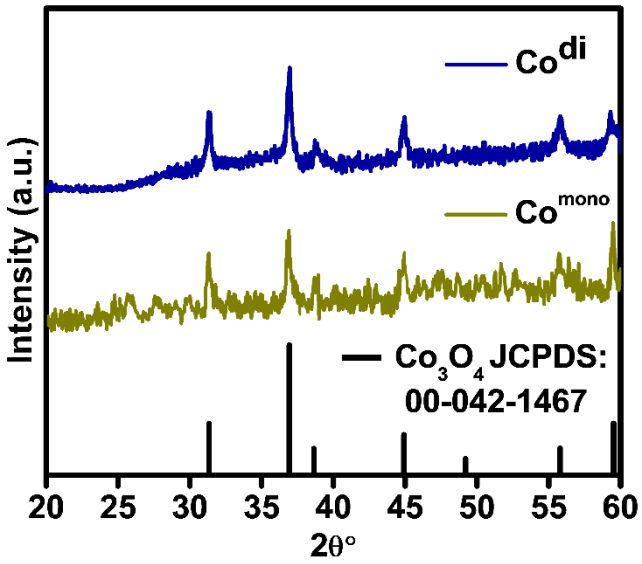

Figure S26: A comparison of the PXRD pattern of post-CPE electrocatalysts, **Co^{mono}** and **Co^{di}** with the PXRD pattern of the standard Co_3O_4 (JCPDS: 00-042-1467).

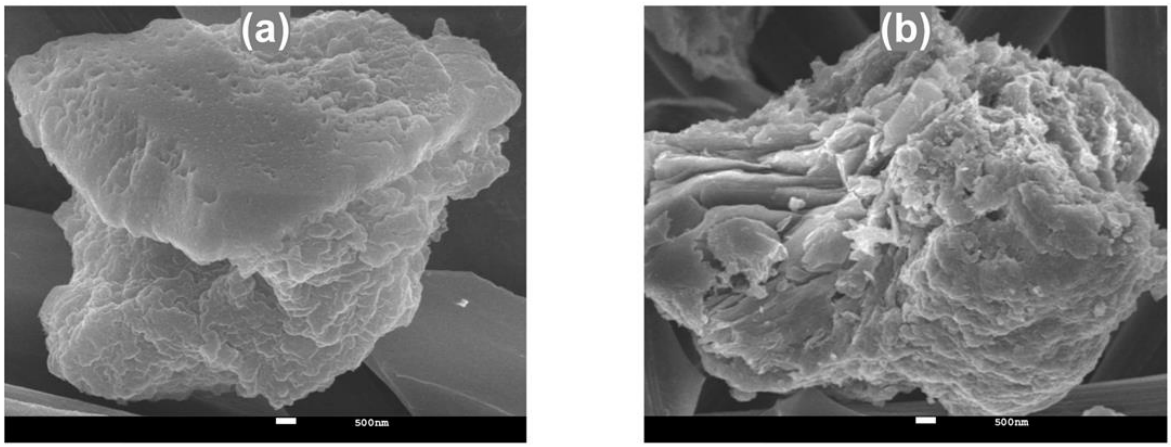

Figure S27: SEM images of post-CPE recovered electrocatalysts: **a) Co** $^{\textbf{mono}}$ and **b) Co** $^{\textbf{di}}$.

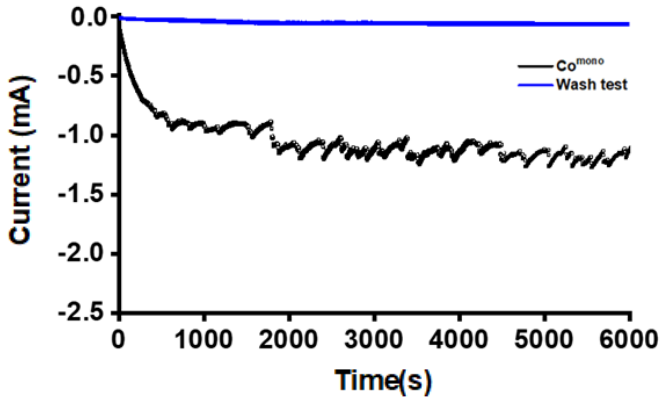

Figure S28: CPE of **Co** $^{\textbf{mono}}$ (black) and wash test of blank working electrode (GC) (blue) in 0.1 M KOH solution for 6000 sec at -0.49 (V vs. RHE).

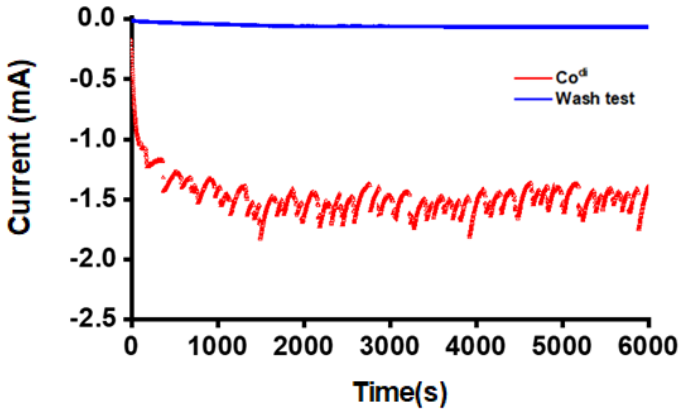

Figure S29: CPE of **Co** ^{di} (red) and wash test of blank working electrode (GC) (blue) in 0.1 M KOH solution for 6000 sec at -0.49 (V vs. RHE).

C.TABLE

Table S1: Crystallographic parameters of Co^{mono} and Co^{di}.

Crystallographic refinement parameters	**Co^{mono}**	**Co^{di}**
CCDC number	**2290443**	**2290444**
Empirical formula	$C_{128}H_{124}Co_4N_{16}O_{25}S_8$	$C_{46}H_{46}ClCo_2N_3O_{14}$
Formula weight	2778.62	1018.17
Temperature, K	250	100
Crystal system	Monoclinic	Monoclinic
Space group	*I2/a*	$P2_1/n$
Unit cell dimensions(Å,)	a = 14.0342(3) b = 12.2099(2) c = 37.0604(9) α =90 ß =97.604(2) γ =90	a = 15.8373(5) b = 19.2808(5) c = 15.9078(5) α = 90 ß = 117.330(4) γ = 90
Volume ($Å^3$)	6294.7(2)	4315.3(3)
Z	2	4
Density (calculated), g/cm^3	1.466	1.567
Absorption coefficient(mm^{-1})	5.952	0.906
F(000)	2880	2104
Reflections collected	25376	49383
Independent reflections	6530	10768
R(int)	0.095	0.057

Goodness-of-fit on F^2	1.06	1.06
R indices (all data)	R = 0.0693 wR2= 0.2035	R = 0.0365 wR2 = 0.0854
Largest diff. peak and hole(e. $Å^{-3}$)	-0.88 and 0.79	-0.67 and 0.37

Table S2. Bond distances and bond angles of Co^{mono}

Co^{mono}	**Bond length (Å)**	**Co^{mono}**	**Bond length(Å)**
Co1−O2	1.999(3)	Co1−O6	2.349(3)
Co1−O3	2.322(3)	Co1−N3	2.028(4)
Co1−O5	2.037(3)	Co1−N4	2.028(3)
Co^{mono}	**Bond angles (°)**	**Co^{mono}**	**Bond angles (°)**
O2-Co1-O3	73.78(10)	N3-Co1-O3	174.04(12)
O2-Co1-O5	149.09(11)	N3-Co1-O5	95.62(12)
O2-Co1-O6	82.43(10)	N3-Co1-O6	87.96(12)
O2-Co1-N3	101.39(13)	N4-Co1-O3	82.64(12)
O2-Co1-N4	97.12(13)	N4-Co1-O5	104.54(13)
O3−Co1−O6	87.93(10)	N4-Co1-O6	170.28(13)
O5-Co1-O3	87.25(10)	N4-Co1-N3	101.62(14)
O5-Co1-O6	72.51(10)		

Table S3. Bond distances and bond angles of Co^{di}

Co^{di}	**Bond length (Å)**	**Co^{di}**	**Bond length(Å)**
Co1–O2	1.96(12)	Co2–O5	2.0831(13)
Co1–O3	2.182(12)	Co2–O8	2.0397(13)
Co1–O5	2.082(13)	Co2–O9	2.2309(14)
Co1–O8	2.0593(13)	Co2–O10	2.0842(14)
Co1–O7	2.412	Co2–N2	2.1026(16)
Co1–N1	2.0264(17)	Co2–N3	2.0585(15)
Co^{di}	**Bond angles (°)**	**Co^{di}**	**Bond angles (°)**
O2–Co1–O3	169.83(6)	O5–Co2–O8	79.86(5)
O2–Co1–O5	94.53(5)	O5–Co2–O9	114.92(5)
O2–Co1–O8	94.02(5)	O5–Co2–O10	85.29(5)
O2–Co1–N1	93.65(6)	O5–Co2–N2	85.06(6)
O2–Co1– O7	87.72	O5–Co2–N3	170.08(6)
O3–Co1–O5	87.51(5)	O8–Co2–O9	163.46(5)
O3–Co1–O8	96.15(5)	O8–Co2–O10	92.42(5)
O3–Co1–N1	77.05(6)	O8–Co2–N2	106.87(6)
O3–Co1– O7	95.53	O8–Co2–N3	90.40(6)
O5–Co1–O8	79.44(5)	O9–Co2–O10	81.96(5)
O5–Co1–N1	124.36(5)	O9–Co2–N2	82.78(6)
O5–Co1– O7	149.83	O9–Co2–N3	74.50(5)
O7–Co1–O8	70.40	O10–Co2–N2	156.50(6)
O7–Co1– N1	85.39	O10–Co2–N3	93.31(6)
O8–Co1–N1	154.24(5)	N2–Co2–N3	99.70(6)

Table S4. Hydrogen bond lengths (Å) and angles (°) for Co^{mono}.

D–H···A	*d*(D–H)	*d*(H···A)	*d*(D···A)	∠(DHA)	Symmetry
N1–H1 ..O1	0.87	2.2	2.581(4)	106.0	-
N1– H1 ..O2	0.87	1.84	2.564(4)	139.0	-
N2–H2..O4	0.87	2.24	2.593(4)	104.0	-
N2–H2 ..O5	0.87	1.92	2.614(4)	136.0	-
O7–H7A ..S2	0.86	2.79	3.289(2)	118.0	1/2-x,-1+y,1-z
O7–H7B ..S2	0.86	2.65	3.289(2)	132.0	x,-1+y,z
C11–H11..S1	0.94	2.83	3.680(5)	151.0	1/2-x,y,1-z
C13–H13..O7	0.94	2.58	3.228(9)	126.0	-
C16–H16B ..O2	0.97	2.55	3.153(5)	121.0	-
C23–H23 .. S1	0.94	2.83	3.584(4)	138.0	1/2-x,3/2-y,1/2-z

Table S5. Hydrogen bond lengths (Å) and angles (°) for Co^{di}.

D–H···A	*d*(D–H)	*d*(H···A)	*d*(D···A)	∠(DHA)	Symmetry
O10–H10..O1	0.862(16)	2.459(16)	3.121(2)	134.1(12)	-
O10–H10..O2	0.862(16)	1.805(16)	2.6045(19)	153.5(14)	-
C1–H1B..O7	0.98	2.53	3.274(3)	132.00	1/2+x,1/2-y,1/2+z
C23–H23..O6	0.95	2.4	2.831(3)	107.00	-
C30–H30A..O12	0.98	2.59	3.515(3)	158.0	-x,1-y,1-z
C30–H30A ..O13A	0.98	2.55	3.36(3)	140.0	-x,1-y,1-z
C33–H33..O13A	0.95	2.54	3.39(3)	149.0	1/2+x,1/2-y,1/2+z
C40–H40..O11	0.95	2.42	3.331(3)	160.0	1/2-x,-1/2+y,3/2-z
C45–H45A ..O10	0.98	2.57	3.349(3)	136.0	1-x,1-y,2-z
C46–H46B..O9	0.98	2.6	3.168(3)	117.0	-

Table S6: Comparison of magnetic properties of reported dinuclear Co (II) Complexes:

Complex	Coupling	d(Å)	$^{\gamma}$(deg)	$^{\delta}$(deg)	Ref
$[Co_2(L)_2(acac)_2(H_2O)]$ HL=(4-methyl-2-formyl-6-(((2-trifluoromethyl)phenyl)methyl iminomethyl) phenol)	F	3.127	97.0 97.6	63.0 30.6	[16]
$[CoL(phen)]_2$ H_2L=1H-anthra[1,2-d]imidazol-6,11-dione-2-[2-hydroxyphenyl]	F	3.106	97.1	62.7 67.9	[17]
$[Co_2(L)_2(N_3)_2]$ HL=4-methyl-2,6-*bis*(3,5-dimethyl-1H-pyrazol-1-yl)methyl)phenol	F	3.198	99.5 99.9	35.6 34.9	[18]
$[Co(L)(acac)]_2$ HL=$(\mu\text{-}NCN_{imidazolidine})_2(\mu\text{-}O_{phenolate})_2$	F	2.893	90.1	89.0	[19]
$[Tl_2Co(OC_8F_6H_3)_4 \cdot toluene]_2$	F	3.251	97.1	65.9	[20]
$[Co_2^{di}(L)_3(CH_3OH)]\ ClO_4$ HL=2-methoxy-6-(((2-methoxyphenyl)imino)methyl) phenol	F	3.129	99.51 97.38	41.32 36.38	This work

Table S7: Temperature-dependent conductivity of Co^{mono} and Co^{di}

Temperature (K)	Conductivity (Sm^{-1}) of Co^{mono}	Conductivity (Sm^{-1}) of Co^{di}
300	3.90×10^{-5}	6.89×10^{-4}
315	4.31×10^{-5}	7.71×10^{-4}
330	4.73×10^{-5}	8.48×10^{-4}
345	5.16×10^{-5}	9.31×10^{-4}

Table S8: Schottky Diode Parameters

Sample	d(V)/d(lnI) vs. I Graph		H(I) vs. I Graph	
	Ideality Factor (η)	**Series Resistance (R_S) (Ohm)**	**Barrier Height (ϕ_b) (eV)**	**Series Resistance (R_S) (Ohm)**
Co^{di}	1.85	204.86	0.62	220.35
Co^{mono}	2.35	1895.60	0.67	2148.03

Table S9: SCLC/Charge Transport Parameters

Sample Name	**ε_r**	**Carrier mobility (μ) $m^2v^{-1}s^{-1}$**	**Transit Time (τ) (Sec)**
Co^{mono}	0.4652	2.02×10^{-5}	7.77×10^{-9}
Co^{di}	0.7513	9.21×10^{-5}	1.70×10^{-9}

Table S10: Electrochemical parameter

Catalyst	Overpotential(η) @ 10mA/cm^2	Tafel slope (mV/dec)	TOF(s^{-1})	Onset (V)	C_{dl} (μF)	ECSA (cm^2)	R_f
Co ^{mono}	574	115	0.093	0.456	2.50	0.091	1.29
Co ^{di}	525	146	0.503	0.376	3.46	0.126	1.78

Table S11: Electrochemical parameters before and after CPE

Parameter	Co ^{mono} Before CPE	Co ^{mono} After CPE		Co ^{di} Before CPE	Co ^{di} After CPE
Overpotential (η) @ 10mA/cm^2	574	426		525	412
Onset (V)	0.456	0.263		0.376	0.195

References

(1) Kumar Mudi, P.; Bandopadhyay, N.; Joshi, M.; Shit, M.; Paul, S.; Roy Choudhury, A.; Biswas, B. Schiff Base Triggering Synthesis of Copper(II) Complex and Its Catalytic Fate towards Mimics of Phenoxazinone Synthase Activity. *Inorganica Chim. Acta* **2020**, *505* (December 2019), 119468. https://doi.org/10.1016/j.ica.2020.119468.

(2) Mudi, P. K.; Singla, L.; Chamuah, A.; Bhattacharya, S.; Biswas, A. R. C. B. Schiff Base Driven Denticity-Fluctuated Structural Assortment of Zinc-Pseudohalide Complexes: Synthesis, Structures and Electrical Transport Properties. *CrystEngComm* **2022**, *24*, 2418–2428. https://doi.org/https://doi.org/10.1039/D1CE01646F.

(3) Kundu, S.; Saha, S.; Panda, S. J.; Purohit, C. S.; Biswas, B. Tailor-Made Isostructural Copper(Ii) and Nickel(Ii) Complexes with a Newly Designed (N,N)-Donor Scaffold as Functional Mimics of Alkaline Phosphatase. *New J. Chem.* **2023**, *47* (12), 5894–5902. https://doi.org/10.1039/d2nj06127a.

(4) Debnath, A.; Diyali, S.; Das, M.; Panda, S.; Mondal, D.; Dhak, D.; Purohit, C. S.; Roy, P. P.; Biswas, B. Harnessing the Hydrogen Evolution Reaction (HER) through the Electrical Mobility of an Embossed Ag(i)-Molecular Cage and a Cu(Ii)-Coordination Polymer. *Dalt. Trans.* **2023**, *52* (26), 8850–8856. https://doi.org/https://doi.org/10.1039/D3DT01073B.

(5) SMART & SAINT Software Reference Manual, Version 6.45. Bruker Analytical X-Ray Systems, Inc., Madison.

(6) Sheldrick, G. . *SADABS, Program for Area Detector Adsorption Correction*; Institute for Inorganic Chemistry, University of Gottingen, Germany., 1996.

(7) Sheldrick, G. M. Crystal Structure Refinement with SHELXL. *Acta Crystallogr. Sect.*

C Struct. Chem. **2015**, *71*, 3–8. https://doi.org/10.1107/S2053229614024218.

(8) Rhoderick, E. H.; Williams, R. H. *Metal-Semiconductor Contacts*, 2nd ed.; Clarendon Press ; Oxford University Press: Oxford England New York, 1988.

(9) S. M, S. *Physics of Semiconductor Devices*; Wiley: New York, 1981; Vol. 23.

(10) Sil, S.; Dey, A.; Datta, J.; Das, M.; Jana, R.; Halder, S.; Dhar, J.; Sanyal, D.; Ray, P. P. Analysis of Interfaces in Bornite (Cu5FeS4) Fabricated Schottky Diode Using Impedance Spectroscopy Method and Its Photosensitive Behavior. *Mater. Res. Bull.* **2018**, *106* (June), 337–345. https://doi.org/10.1016/j.materresbull.2018.06.016.

(11) Das, M.; Datta, J.; Dey, A.; Jana, R.; Layek, A.; Middya, S.; Ray, P. P. One Step Hydrothermal Synthesis of a RGO-TiO2 Nanocomposite and Its Application on a Schottky Diode: Improvement in Device Performance and Transport Properties. *RSC Adv.* **2015**, *5* (123), 101582–101592. https://doi.org/10.1039/c5ra17795b.

(12) Blom, P.; de Jong, M.; van Munster, M. Electric-Field and Temperature Dependence of the Hole Mobility in Poly(p-Phenylene Vinylene). *Phys. Rev. B - Condens. Matter Mater. Phys.* **1997**, *55* (2), R656–R659. https://doi.org/10.1103/PhysRevB.55.R656.

(13) Middya, S.; Layek, A.; Dey, A.; Datta, J.; Das, M.; Banerjee, C.; Ray, P. P. Role of Zinc Oxide Nanomorphology on Schottky Diode Properties. *Chem. Phys. Lett.* **2014**, *610–611*, 39–44. https://doi.org/10.1016/j.cplett.2014.07.003.

(14) Das, D.; Das, M.; Sil, S.; Sahu, P.; Ray, P. P. Effect of Higher Carrier Mobility of the Reduced Graphene Oxide-Zinc Telluride Nanocomposite on Efficient Charge Transfer Facility and the Photodecomposition of Rhodamine B. *ACS Omega* **2022**, *7* (30), 26483–26494. https://doi.org/10.1021/acsomega.2c02472.

(15) Datta, J.; Das, M.; Sil, S.; Kumar, S.; Dey, A.; Jana, R.; Bandyopadhyay, S.; Ray, P. P. Improvement of Charge Transport for Hydrothermally Synthesized Cd0.8Fe0.2S over

Co-Precipitation Method: A Comparative Study of Structural, Optical and Magnetic Properties. *Mater. Sci. Semicond. Process.* **2019**, *91* (November 2018), 133–145. https://doi.org/10.1016/j.mssp.2018.11.010.

(16) Song, X. J.; Xue, X. M. Study on the Magneto-Structural Correlation of a New Dinuclear Cobalt(II) Complex with Double μ-Phenoxo Bridges. *ACS Omega* **2020**, *5* (14), 8347–8354. https://doi.org/10.1021/acsomega.0c00853.

(17) Casanova, I.; Durán, M. L.; Viqueira, J.; Sousa-Pedrares, A.; Zani, F.; Real, J. A.; García-Vázquez, J. A. Metal Complexes of a Novel Heterocyclic Benzimidazole Ligand Formed by Rearrangement-Cyclization of the Corresponding Schiff Base. Electrosynthesis, Structural Characterization and Antimicrobial Activity. *Dalt. Trans.* **2018**, *47* (12), 4325–4340. https://doi.org/10.1039/c8dt00532j.

(18) Alam, R.; Pal, K.; Shaw, B. K.; Dolai, M.; Pal, N.; Saha, S. K.; Ali, M. Synthesis, Structure, Catalytic and Magnetic Properties of a Pyrazole Based Five Coordinated Di-Nuclear Cobalt(II) Complex. *Polyhedron* **2016**, *106*, 84–91. https://doi.org/10.1016/j.poly.2015.12.062.

(19) Fondo, M.; Doejo, J.; García-Deibe, A. M.; Sanmartín-Matalobos, J.; Vicente, R.; El-Fallah, M. S.; Amoza, M.; Ruiz, E. Predetermined Ferromagnetic Coupling via Strict Control of M-O-M Angles. *Inorg. Chem.* **2016**, *55* (22), 11707–11715. https://doi.org/10.1021/acs.inorgchem.6b01739.

(20) Petersen, M. V.; Iqbal, A. H.; Zakharov, L. N.; Rheingold, A. L.; Doerrer, L. H. Fluorinated Phenolates in Monomeric and Dimeric Co(II) Compounds. *Polyhedron* **2013**, *52*, 276–283. https://doi.org/10.1016/j.poly.2012.09.032.